Accepted for publication by: **Computers and Mathematics with Applications**

Lattice Boltzmann simulation of water and gas flow in porous gas diffusion layers in fuel cells reconstructed from micro-tomography

Yuan Gao[a], Xiaoxian Zhang[a], Pratp Rama[b], Rui Chen[c], Hossein Ostadi[d], Kyle Jiang[d]

[a] School of Engineering, University of Liverpool, Liverpool, L69 3GH, UK

[b] Intelligent Energy Ltd., Loughborough, LE11 3GR, UK

[c] Department of Aeronautical and Automotive Engineering, Loughborough University, Loughborough, LE11 3TU, UK

[d] School of Mechanical Engineering, University of Birmingham, Birmingham, B15 2TT, UK

Keywords:

Gas diffusion layer, Lattice Boltzmann method, Two-phase flow, X-ray computed tomography, Hydrophobicity

Abstract

The porous gas diffusion layers (GDLs) are key components in hydrogen fuel cells. During their operation the cells produce water at the cathode, and to avoid flooding, the water has to be removed out of the cells. How to manage the water is therefore an important issue in fuel cell design. In this paper we investigated water flow in the GDLs using a combination of the lattice Boltzmann method and X-ray computed tomography at the micron scale. Water flow in the GDL depends on water–air surface tension and hydrophobicity. To correctly represent the water–gas surface tension, the formations of water droplets in air were simulated, and the water–gas surface tension was obtained by fitting the simulated results to the Young–Laplace formula. The hydrophobicity is represented by the water–gas fabric contact angle. For a given water–gas surface tension the value of the contact angle was determined by simulating the formations of water droplets on a solid surface with different hydrophobicity. We then applied the model to simulate water intrusion into initially dry GDLs driven by a pressure gradient in attempts to understand the impact of hydrophobicity on water distribution in the GDLs. The structures of the GDL were acquired by X-ray micro-tomography at a resolution of 1.7 microns. The simulated results revealed that with an increase in hydrophobicity, water transport in GDLs changes from piston-flow to channelled flow.

1. Introduction

Hydrogen fuel cells have attracted increased attention over the past few years because of their zero emission. During their operation, the cells produce water at the cathode. Whilst the presence of some water in the cathode is essential to keep the cell membrane humid so as to efficiently conduct protons from the anode to the cathode, excessive accumulation of water could result in flooding at the cathode and hence deteriorate the cell's performance. As such, how to effectively manage the water is an essential issue in fuel cell design.

The key components in fuel cells are porous gas diffusion layers (GDLs). The GDLs provide not only mechanical support to the cells, but also pathways for gases to move from gas-supply channels to catalyst layers where the electrochemical reactions take place to release the electrons from hydrogen. For the GDL at the cathode, it also needs to drain liquid water produced during the electrochemical reaction. Therefore, the cathode GDL has to provide pathways for both liquid water and gases to move simultaneously but in opposite directions. In practice, the GDL is often made hydrophobically heterogeneous so as to force water into a few channels, thereby leaving some space for gases to move through in the opposite direction from the gas-supply channel to the catalyst layer. As a result, spatial distribution of the water in the GDL controls gas flow and hence fuel cell performance. Because of its opaque nature, water distribution in GDLs is difficult to visualise. The existing work on water management in fuel cells is largely based on macroscopic models to predict saturation [1]. Whilst the saturation tells the percentage of pores that are filled by water, what controls gas flow in GDLs is the connectedness of the pores that remain unoccupied by water. The development in imaging technology over the past decade has been overcoming this barrier, and there has been increased research in the use of neutron imaging to visualise liquid water distribution in operating cells [2]. In our previous work, we have successfully visualised the 3D structure of the GDL at a resolution less than one micron using both computed X-ray tomography and FIB technology [3]. This, in combination with computational fluid dynamics, such as the lattice Boltzmann (LB) method and smooth particle hydrodynamic methods, has made simulation of water flow and water distribution in GDLs feasible at scales as fine as a few hundred nanometers [4].

Several LB models have been developed since the 1980s to simulate two-phase flow. The earliest lattice-type two-phase model is the approach proposed by Rothman and Keller [5] (referred to as the RK model hereafter) based on the lattice gas algorithm (LGA). Because of its nature, the RK model inherited some drawbacks of the LGA such as numerical noises. Gunstensen et al. [6,7] developed the LGA-based RK model into the LB model based on the concept of McNamara and Zanetti [8] using a linearised collision operator proposed by Higuera and Jimenez [9]. The RK model used two coloured particles to represent the two phases, and a perturbation to approximately recover Laplace's law at the fluid interface; it overcomes some drawback of the original RK model, including lack of Galilean invariance and

statistical noise. The drawback of this model is that it is not rigorously based upon thermodynamics and is thus difficult to incorporate microscopic physical processes [10]. In addition, the pressure in this model is velocity-dependent, and the linearised collision operator is not computationally efficient [11]. Recently, Ahrenholz et al. has combined the RK model with the multiple-relaxation time LB model to simulate unsaturated water flow in glass bead columns [12].

Another two-phase LB model is the method proposed by Shan and Chen [13,14] (referred to as the SC model hereafter) and its modified versions [15,16]. In the SC model, a nonlocal interaction force between particles of different fluids at neighbouring lattices is introduced, similar to the van der Waals attraction between fluid particles. Phase separation occurs when the attractive interaction is strong enough. Hou et al. [17] compared the RK and SC models, finding that the SC model is superior to the RK model in reducing numerical noise and handling fluids with contrasting densities. Recent development in the RK model has shown that such spurious noise can be reduced or even eliminated by using Latva-Koko's operator in the re-recolour step [18]. This could make the RK model more competitive than the SC model as revealed in a comparative study by Huang et al. [19]. Both the RK model and the SC model are based on the same lattice Boltzmann equation, thus they are efficient for parallelisation and easy to handle complicated boundaries. The SC model is a phenomenally-based model and does not conserve momentum locally. As such, some key parameters such as fluid–fluid surface tension cannot be derived a priori, and have to be estimated based on numerical experiments. Also, the SC model cannot handle fluids with large density ratios.

The third two-phase LB model is the free-energy approach developed by Swift et al. [20,21]. In this model, the equilibrium distribution function in the classical LB model for ideal gases is modified so as to make it capable of simulating two-phase flow. The free-energy LB model conserves mass and momentum both locally and globally, and is formulated to account for the equilibrium thermodynamics of non-ideal gases. The major drawback of this model is the unphysical non-Galilean invariance for the viscous terms in the macroscopic Navier–Stokes equation.

The above three models are widely used in the literature to simulate two-phase flow with each having pros and cons as they are not directly derived from the kinetic theory. He et al. proposed a two-phase model by linking the LB model to the Boltzmann equation in the kinetic theory [22]. However, numerical experiences revealed that this method is susceptible to numerical instability, particularly for fluids with large density and viscosity ratios. To improve its numerical stability, Lee and Lin [23] developed a stable discretisation method to solve the lattice Boltzmann equation proposed by He et al. [22]; results showed that the improved discretisation method significantly enhances stability and can hence handle fluids with density ratios as high as 1:1000. Other two-phase models developed over the past decade for simulating fluids with high density ratios include the method of Zheng et al. [24] and of Inamuro [25]. One drawback of these methods is that they need to calculate

spatial derivatives up to second order, making them cumbersome to simulate two-phase flow in porous media because of the complicated fluid–solid boundary. Furthermore, most two-phase flow in porous media is dominated by capillary forces. As a result, both the RK and SC models can offer good solutions and are widely used in practice.

There has been an increase in the use of LB models to simulate two-phase flow in fuel cells over the past few years. For example, Mukherjee and Wang [26] studied the influence of pore structure and GDL wettability on water transport and interfacial dynamics in stochastically constructed catalyst layers and gas diffusion layers in fuel cells. Niu et al. [27] did similar work in attempts to examine water flow in stochastically reconstructed GDLs and the dependence of relativepermeability for both air and water on water saturation. For water flow in the gas-supply channel, Hao and Cheng [28] simulated the dynamic behaviour of a water droplet under different flow conditions. The purpose of this paper is to investigate the impact of hydrophobicity on water intrusion in the GDLs using the SC model. The paper is organised as follows. We first describe the SC model in Section 2, and then explain how we determined the water–gas surface tension and the contact angle in Section 3. The implication and limitations of the model are discussed in Section 4.

2. Methodology

The lattice Boltzmann method consists of two steps: The first step is to calculate the collision between fluid particles, and the second step is to stream the fluid particles. In this paper, we consider two fluids and the evolution of the fluid–particle distribution functions for each fluid is described by the following equation [29]:

$$\int_a^k (x_i + c_a \Delta t, t + \Delta t) - \int_a^k (x_i, t) = -MSM^{-1}\left(\int_a^k (x_i, t) - \int_a^{k(eq)} (x_i, t)\right) \quad (1)$$

where x_i is a position vector, t is time, $\int_a^k (x_i, t)$ is the particle distribution function of fluid k, moving in the ath direction with velocity c_a, $\int_a^{k(eq)} (x_i, t)$ is the equilibrium distribution functions of fluid k, Δt is a time step during which the particle moves from one lattice into another. In this paper, we used the D3Q19 model in which, as shown in Fig. 1, the lattice velocity c_a is defined as follows:

$$c_a = \begin{cases} \frac{(0,0,0)c}{\Delta t} & a = 0 \\ \frac{(\pm 1,0,0)c}{\Delta t}, \frac{(0,\pm 1,0)c}{\Delta t}, \frac{(0,0,\pm 1)c}{\Delta t} & a = 1, \dots, 6 \\ \frac{(\pm 1,\pm 1,0)c}{\Delta t}, \frac{(\pm 1,0,\pm 1)c}{\Delta t}, \frac{(0,\pm 1,\pm 1)c}{\Delta t} & a = 7, \dots, 18 \end{cases} \quad (2)$$

where c is the side length of each cubic lattice. In Eq. (1), $S = -M^{-1}S^k M$ is a matrix describing the collision between fluid particles, whereM is a transform matrix that transforms the distribution functions into moments, and S^k is a diagonal matrix to perform the relaxation collision in moment space. The terms of S^k are given by

$$S^k = diag\left(S_0^k, S_1^k, \ldots, S_{18}^k\right) \tag{3}$$

where S_1^k, S_2^k, S_9^k, S_{10}^k, S_{11}^k, S_{12}^k, S_{13}^k, S_{14}^k, S_{15}^k are related to the kinematic viscosity of fluid k12]. As proven in the literature, a good choice for the values of the relaxation parameters in Eq. (3) are [30,31]:

$$\begin{gathered} S_0^k = S_2^k = S_5^k = S_7^k = 0 \\ S_1^k = S_3^k = S_9^k = S_{10}^k = S_{11}^k = S_{12}^k = S_{13}^k = S_{14}^k = S_{15}^k = 1/\tau_k \\ S_4^k = S_6^k = S_8^k = S_{16}^k = S_{17}^k = S_{18}^k = 8\left((2 - 1/\tau_k)/(8 - 1/\tau_k)\right) \end{gathered} \tag{4}$$

where τ_k is a dimensionless parameter that is related to the viscosity of fluid μ_k in that $\mu_k = c^2(\tau_k - 0.5)/3\Delta t$. In the above LB model, the collision was calculated in the moment space as follows:

$$\int_a^k (x_i + c_a\Delta t, t + \Delta t) = \int_a^k (x_i, t) - M^{-1}S^k\left(m_a^k(x_i, t) - m_a^{k(eq)}(x_i, t)\right) \tag{5}$$

Where $m_a^k = M \times \int_a^k$ is the moment and $m_a^{k(eq)} = M \times \int_a^{k(eq)}$. The transformation matrix M was given in detail in [29]. The equilibrium distribution functions for the D3Q19 model are given by

$$\begin{gathered} \int_a^{k(eq)} = \omega_a\rho_k\left[1 - \frac{3}{2}\frac{u_k^{eq}\cdot u_k^{eq}}{c_s^2}\right] \quad a = 0, \\ \int_a^{k(eq)} = \omega_a\rho_k\left[1 + 3\frac{c_a u_k^{eq}}{c_s^2} + \frac{9}{2}\frac{\left(c_a u_k^{eq}\right)^2}{c_s^2} - \frac{3}{2}\frac{u_k^{eq}\cdot u_k^{eq}}{c_s^2}\right] \quad a = 1, \ldots, 18 \end{gathered} \tag{6}$$

where $\omega_a =$ 1/1/3, $\omega_{1,\ldots,6} =$ 1/18, $\omega_{7,\ldots,18} =$ 1/36, $c_s^2 = c^2/3\Delta t^2$. The equilibrium velocity u_k^{eq} in Eq. (6) for fluid k is determined by:

$$\rho_k u_k^{eq} = \rho_k u' + \tau_k F_k \tag{7}$$

where u' is bulk velocity and is calculated by

$$u' = \frac{\sum_k \rho_k u'/\tau_k}{\sum_k \rho_k/\tau_k} \tag{8}$$

in which ρ_k is the density of fluid k and calculated by $\rho_k = \sum_{i=0}^{18} \int_a^k$, and u_k is the velocity of fluid k and calculated by $\rho_k u_k = \sum_{i=0}^{18} \int_a^k c_a$. F_k is the net force acting on fluid k, including fluid–fluid interaction F_1^k and fluid–solid interaction F_2^k. That is,

$$F_k = F_1^k + F_2^k \tag{9}$$

The fluid–fluid reaction is calculated as follows:

$$F_1^k(x) = -\rho_k(x)\sum_{k'}\sum_k G_{k\overline{k}}(x, x')\rho_{\overline{k}}(x')(x' - x) \tag{10}$$

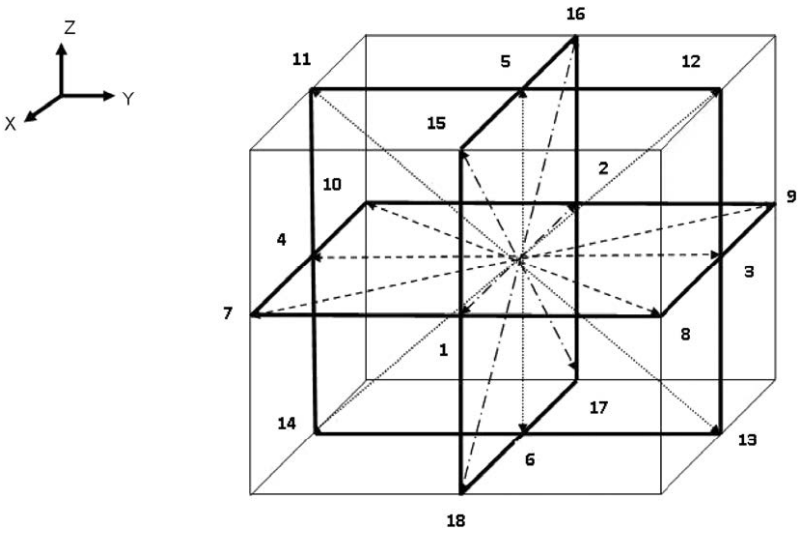

Figure 1: Structure of the D3Q19 LB model

where $G_{k\bar{k}}(x,x')$ is the Green's function and satisfies $G_{k\bar{k}}(x,x') = G_{\bar{k}k}(x,x')$. In this paper, it is calculated by

$$G_{k\bar{k}}(x,x') = \begin{cases} g_{k\bar{k}}|x-x'| = c \\ g_{k\bar{k}}/2|x-x'| = \sqrt{2c} \\ 0\ otherwise \end{cases} \tag{11}$$

where $g_{k\bar{k}}$ represents the strength of the fluid–fluid reaction. The fluid–solid reaction is modelled by

$$F_2^k(x) = -\rho_k(x)G_{ks}(x,x')n_s(x')(x'-x) \tag{12}$$

where $n_s(x')$ is a non-zero constant at the fluid – solid interface and zero otherwise. $G_{ks}(x,x')$ represents fluid – solid interaction strength and defines the wall wettability. To ensure consistency with the fluid–fluid interaction, the fluid–wall interactive strength is described by

$$G_{ks}(x,x') = \begin{cases} g_{ks}|x-x'| = c \\ g_{ks}/2|x-x'| = \sqrt{2c} \\ 0\ otherwise \end{cases} \tag{13}$$

The sign of g_{ks} describes a hydrophobic or hydrophilic solid.

A material in a 3D image acquired by X-ray tomography is represented by a number of cubic elements. The 3D image is a gray photo with each element represented by an attenuation number ranging from 0 to 255, depending on the components in the element. A binary 3D structure is obtained from the gray image using the threshold method in which any elements with attenuation number less than the threshold are thought of as pores, and those with attenuation number higher than the threshold are classified as fabric solid. Because of this nature of tomography, any curved solid surface is approximated by a staircase surface in the 3D X-ray image;

mathematically, this is a first-order approach. Efforts have been made over the past few years to rebuild smooth solid surface based on the zigzag surface in reconstructed images of porous materials for LB simulations [32]. However, for complicated porous materials like the GDLs investigated in this paper, the X-ray images always have errors to represent the void–solid surface due to the resolution limitation of imaging technology. As a result, we did not reprocess the binary X-ray images so as to make the staircase solid surface smooth. Instead, all the simulations used the original binary structures in which both pore and solid were represented by cubes each with a side length of 1.76 μm. All the distribution functions were defined at the centre of the cube, and the fluid–solid boundary was solved by the bounce back method. Because all cubic elements are the same, any particle in an element with its moving direction adjacent to a solid wall will move back to the element after the bouncing-back. Such a treatment is the special case of the method proposed by Bouzidi et al. [33] with the parameter q (Eq. (6) in [33]) being 1/2.

Water intrusion through the image was simulated by applying a pressure drop in one direction; the pressure drop was simulated by imposing one prescribed pressure at the inlet boundary and one prescribed pressure at the outlet boundary, respectively; the other four sides of the 3D image were treated as periodic boundaries in which any particle exiting the image from one side re-enters the image from the opposite side with its mass and momentum remaining unchanged. The prescribed pressures were solved using the method proposed by Zou and He [34].

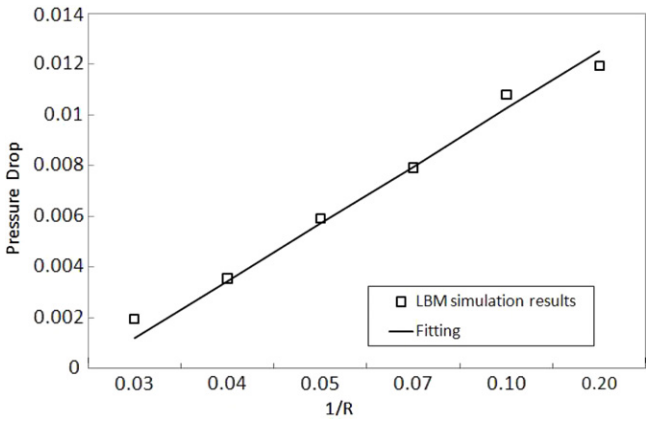

Figure 2: Change of pressure drop across the bubble surface with bubble radius

3. Simulation and results analysis

The measurable parameters at macroscopic scale which control water intrusion in GDL are fluid–fluid surface tension and the fluid–fluid–solid contact angle, whilst the input parameters to the LB model are the fluid–fluid reaction strength parameter $g_{k\bar{k}}$ and the fluid–solid reaction strength parameter gks, which are not measurable. For a given two fluids, their surface tension is fully determined by $g_{k\bar{k}}$, but there is no analytical expression for them. The same applies to the dependence of contact angle on $g_{k\bar{k}}$ and g_{ks}. To establish these relationships, a series of numerical experiments

were carried out to numerically calculate the dependence of the surface tension on $g_{k\bar{k}}$ and the dependence of contact angle on $g_{k\bar{k}}$ and g_{ks}.

3.1. Surface tension

To establish the relationship between surface tension and $g_{k\bar{k}}$ the formation of water droplets with different diameters was simulated in a domain consisting of $50 \times 50 \times 50$ cubic cells; all the boundaries were treated as periodic boundaries. After the two fluids reached steady state, the pressure drop across the fluid–fluid interface was measured. The relationship between the pressure drop ΔP and the radius of the water droplet R is described by the following equation:

$$\Delta P = \frac{\sigma}{R} \tag{14}$$

where σ is the surface tension, and ΔP is the pressure difference across the fluid–fluid interface.

One limitation of the SC model is that it is unable to deal with fluids with large density ratios. For the water–air system investigated in this paper, the density and viscosity ratios are $1:800$ and $1:15$, respectively, which is beyond what the SC model can handle. Water transport in the GDLs is controlled by several forces and to determine which force is in dominance, we estimated the Bond number (ratio of gravity to interfacial tension force), capillary number (ratio of viscous force to interfacial force) and Reynolds number (ratio of inertial force to viscous force). The average pore size in the GDLs is approximately 10 μm. As a result, the ranges of the three numbers are: 1.6×10^{-4} for the Bond number, $2.47 \times 10^{-8} - 1.92 \times 10^{-7}$ for the capillary number, and $2.12 \times 10^{-4} - 1.65 \times 10^{-4}$ for the Reynolds number. This reveals that water flow in the GDL is dominated by the capillary force. For numerical stability, in all the simulations we used $\rho_1 = 0$ and $\rho_2 = 1.0$ inside the initial bubbles and $\rho_1 = 1.0$ and $\rho_2 = 0$ outside the bubbles. The two dimensionless relaxation-time parameters were set to be $\tau_1 = 1.0$ and $\tau_2 = 1.2$ and the dimensionless fluid–fluid interaction coefficient $g_{k\bar{k}}$ was set to be 0.001 in all the simulations. Steady state was deemed to have been achieved when the relative difference of the overall fluid velocity between two adjacent time steps was less than 10^{-6}. Fig. 2 shows the change of pressure drop across the fluid–fluid interface as the radius of the bubbles decreases. It is nicely fitted by Eq. (14); the resulting surface tension is 0.366 in lattice units.

3.2. Contact angle

For a given $g_{k\bar{k}}$ and hence surface tension, the water–air–solid contact angle is determined by g_{ks}. To establish the dependence of the contact angle on g_{ks}, a water droplet with a radius of eight lattice units was placed on a solid wall in the z direction; we then simulated its settlement on the wall by using different fluid–solid reaction parameters g_{ks} . Periodic boundaries were applied to other sides of the computational domain. Simulations were carried out using various g_{ks} ranging from

-0.002 to 0.002; other parameters remain the same as in the surface-tension simulations. Once the two fluids reached steady state, the water–air–solid contact angle was calculated as follows:

$$\tan\theta = \frac{L}{2(R-H)} \tag{15}$$

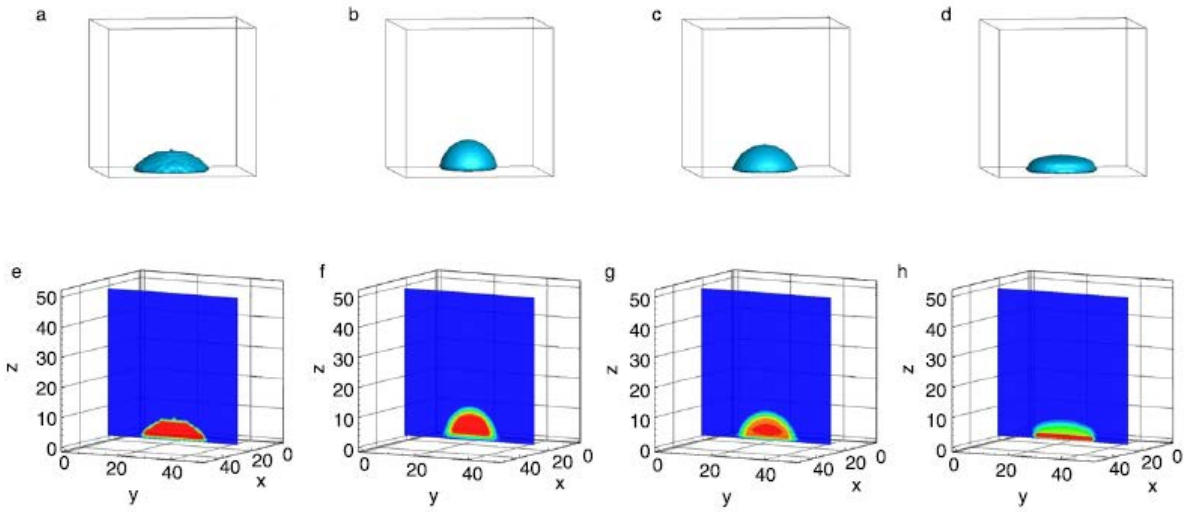

Figure 3: Impact of gks on the shape of the droplets. (a) Initial state; (b) θ > 90° for hydrophobic solid; (c) θ = 90° for neutral solid; (d) θ < 90° for hydrophilic solid. (e)–(h) Density contours associated with (a)–(d)

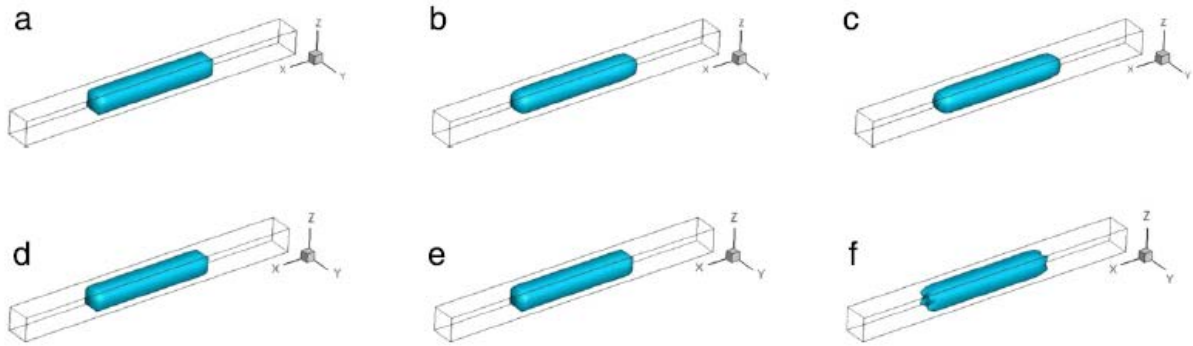

Figure 4: Evaluation of a water droplet in slits. (a)–(c) In hydrophobic slit: (a) initial state, (b) after 5000 time steps and (c) after 5000 time steps. (d)–(e) In hydrophilic slit: (d) initial state, (e) after 5000 steps and (f) after 5000 time steps

The final radius R is evaluated from H and L by

$$R = \frac{H}{2} + \frac{L^2}{8H} \tag{16}$$

where L is the length of the contact area between the droplet and the solid surface, and H is the height of the drop. Fig. 3 shows three contact angles obtained using different fluid–solid interaction parameters g_{ks} and the associated density contours of the droplets. The contact angle increases with g_{ks}; when g_{ks} is negative, the contact angle is less than $90°$ and the solid is hydrophobic; when g_{ks} is positive, the contact angle is greater than $90°$ and the solid is hydrophilic; when g_{ks} is zero, the solid is neutral and the associated contact angle is $90°$.

Fig. 4 shows the water distribution in narrow slits simulated using the model for both hydrophobic and hydrophilic slits.

3.3. Water flow in GDLs

The GDLs used in the simulations were acquired by X-ray micro-tomography at a resolution of 1.76 μm. Because of the limitation of computational power, we only simulated a small portion of the acquired image. The image is shown in Fig. 5, and the size of the image was $50 \times 50 \times 150$ voxels. To mimic water flow in GDLs during cell operation, a pressure drop was applied in the z direction in an initially dry GDL. Driven by the pressure drop, water moved into the GDLs, but the intrusion speed and water distribution in the GDLs change with the pressure drop and the hydrophobicity. The pressure drop was maintained by applying a constant water pressure and zero air pressure at the inlet, and a constant air pressure and zero water pressure at the outlet. Fig. 5(b) shows the initial setup of the simulations.

To investigate the impact of hydrophobicity, we simulated water intrusion into both hydrophobic and hydrophilic GDLs. Figs. 6–9 show the water distribution and the invasion pattern driven by different pressure drops. It is evident that the water intrudes faster as pressure drop increases. Fig. 6 shows the water distribution in both hydrophobic and hydrophilic GDLs driven by a pressure drop of 0.594 kPa. It reveals that at low pressure drop, the invading front of the water overcomes the barrier pressure only at some preferential locations due to the resistance of the capillary force.

It is evident that as the applied pressure drop increases, the water intrudes deep in both hydrophobic and hydrophilic GDLs as shown in Figs. 7–9. However, the water distribution in hydrophobic GDLs differs noticeably from that in hydrophilic GDLs. As the pressure drop increases, water intrusion in the hydrophilic GDLs likes piston-flow, occupying almost all the available pore space as shown in Fig. 9(a), whilst in the hydrophobic GDLs, the water was channelled, leaving a significant space for the air to flow. This has important implications in fuel cell design.

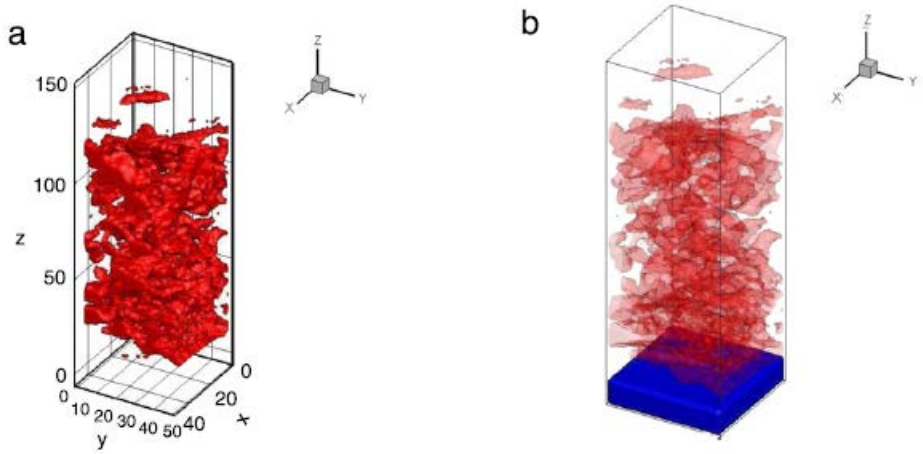

Figure 5: (a) Reconstructed GDL image. (b) Initial condition for water intrusion into a dry GDL

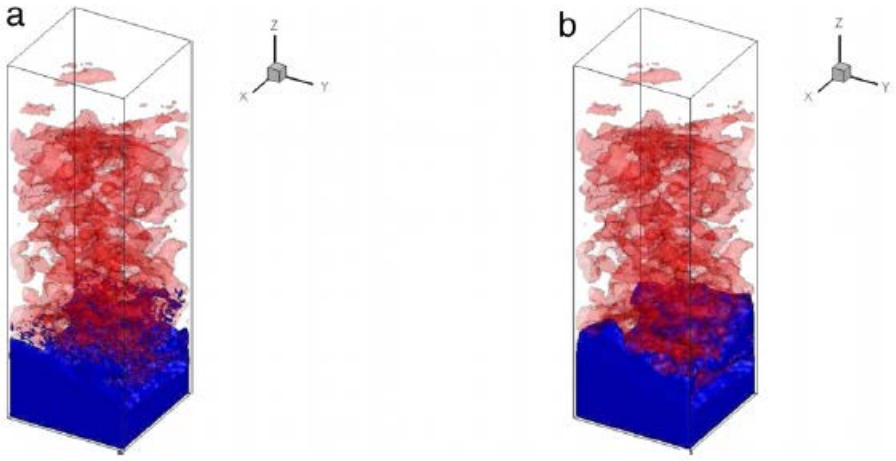

Figure 6: Water intrusion into hydrophilic GDL (a), and hydrophobic GDL (b) under a pressure drop of 0.594 kPa

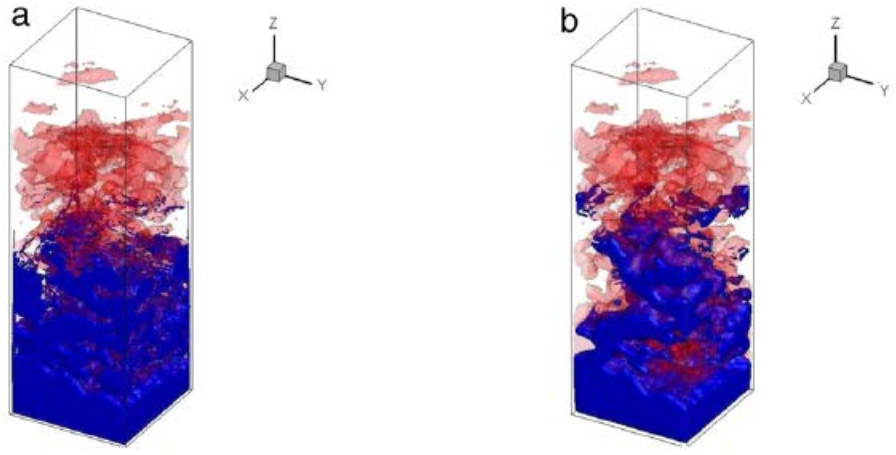

Figure 7: Water intrusion into hydrophilic GDL (a), and hydrophobic GDL (b) under a pressure drop of 2.97 kPa

Fig. 10 further demonstrates the change of saturation under different pressure drops when water intrusion reached steady state in both hydrophobic and hydrophilic GDLs. The results indicated that the saturation increases with the pressure drop for both

hydrophilic and hydrophobic GDLs. However, at low pressure drop, the saturation in the hydrophobic GDL is much lower than the saturation in hydrophilic GDL, and as the pressure drop increases, the difference between hydrophilic and hydrophobic GDLs decreases.

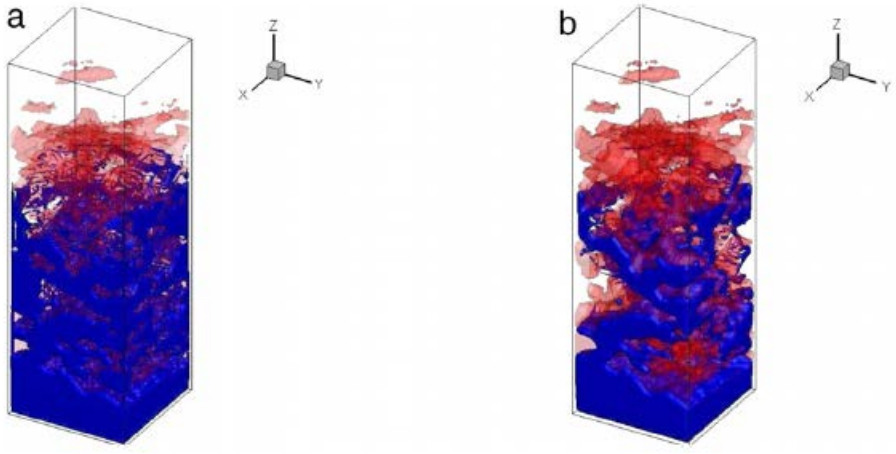

Figure 8: Water intrusion into hydrophilic GDL (a), and hydrophobic GDL (b) under a pressure drop of 5.94 kPa

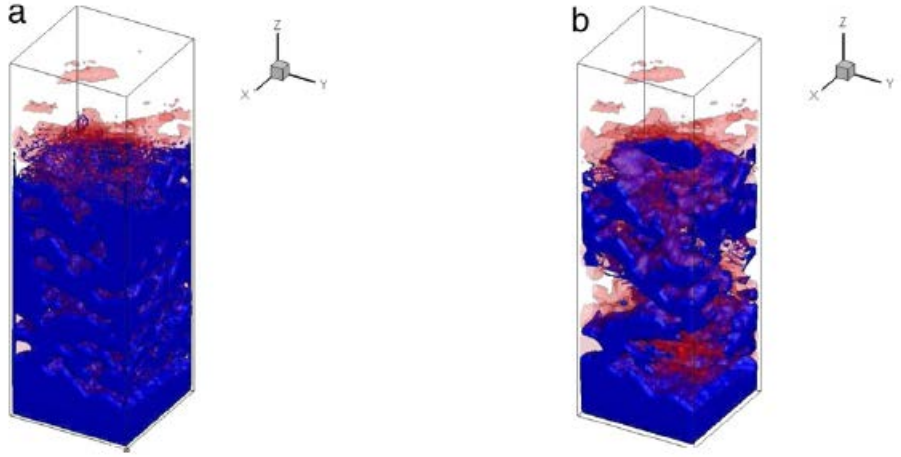

Figure 9: Water intrusion into hydrophilic GDL (a), and hydrophobic GDL (b) under a pressure drop of 11.88 kPa.

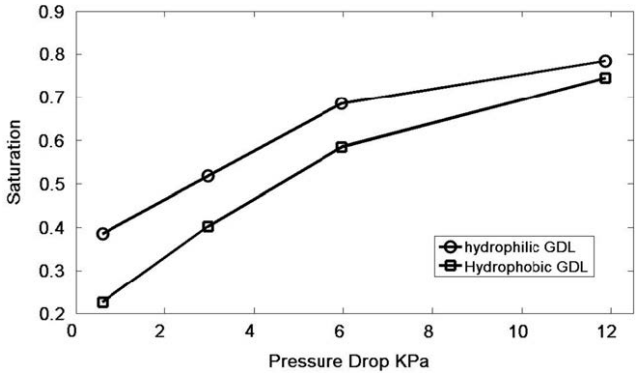

Figure 10: Comparison of water saturation in hydrophilic and hydrophobic GDLs under different pressure drops

4. Summary and conclusions

In this paper we investigated numerically the impact of hydrophobicity on water intrusion in GDLs used in the hydrogen fuel cell industry. The numerical simulations were based on the multiple-relaxation time lattice Boltzmann model. In the simulations, the dependence of water–air surface tension and water–air–solid contact angle on the LB model parameters was established by simulating the formation of water droplets in air and on the top of a solid wall respectively. Simulated results revealed that, under high pressure drop, water intrusion in hydrophobic GDLs is likely to be channelled, bypassing some pores, whilst in the hydrophilic GDLs, water intrusion likes a piston-flow in which water occupies all the pore space. Under low and medium pressure drops, because of the capillary barrier, water in both hydrophilic and hydrophobic GDLs is unsaturated, but water distribution in them is different. In hydrophobic GDLs, the water exists in large pores, whilst in hydrophilic GDLs the water intrudes into small pores first.

We used the SC two-phase model to simulate water intrusion. The SC model is a phenomenal model, solving the fluid–fluid interface by the diffused interface method in which the interface thickness spans several lattices. Therefore, spatial resolution needs to be sufficiently high in order to accurately represent the fluid–fluid interface. For example, a recent study of Yu and Fan [31] reveals that the surface tension estimated by the SC model using different spatial resolutions not only differs significantly but also depends on the value of the relaxation parameters. In fuel cell design, what is interesting is the water distribution when flow reaches a steady state. Furthermore, since water flow in GDLs is dominated by capillary, the two relaxation parameters we used for both fluids were close to unity in the simulations; the water–air surface tension is recovered by adjusting the time step. This naturally overcomes the dependence of surface tension on the relaxation parameters. For the impact of the spatial resolution, the porosity of a typical GDL is approximately 0.8 and the average pore size is 10 μm. The X-ray images were acquired at a very high resolution, 1.7 μm, which should be sufficient for LB simulations. Because of the heterogeneous nature of GDLs, however, it is likely that some fine pores in the GDLs might have been poorly represented in the X-ray image; the impact of such pores on the accuracy of the simulated results is an issue that needs further investigation. In all 3D simulations, there is always a trade-off between solution accuracy and the size of the sample which should be big enough to be representative. Yu and Fan proposed an adaptive mesh method which could be useful to solve this dilemma, using a fine mesh in fine pores and a coarse mesh in big pores [31]. Nonetheless, the results presented in this paper provide some insights into the impact of hydrophobicity on water intrusion in GDLs. The results show that manufacturing hydrophobic GDLs is able to force water into channels, but hydrophobicity makes water difficult to move from GDLs to the gas supply channel. Therefore, in designs, fully hydrophobic GDLs might not be able to improve water management. An alternative is to make GDLs heterogeneously hydrophobic in that some areas are

hydrophilic and some areas are hydrophobic. As such, liquid water can be channelled under both high pressure and low pressure. How to experimentally quantify the heterogeneous hydrophobicity of GDLs and its effect on water flow is under development, and we will present the results in future publications.

Acknowledgements

This research is supported by the UK Technology Strategy Board (TSB Project no. TP/6/S/K3032 H). We acknowledge the kind support from project partners AVL list GmbH, Intelligent Energy Ltd., Johnson Matthey Fuel Cells Ltd., Saati Group Inc. and Technical Fibre Products Ltd.

References

[1] U. Pasaogullari, P.P. Mukherjee, C.Y. Wang, K.S. Chen, Anisotropic heat and water transport in a PEFC cathode gas diffusion layer, J. Electrochem. Soc. 154 (8) (2007) B823–B834.

[2] R. Mukundan, R.L. Borup, Visualising liquid water in PEM fuel cells using neutron imaging, Fuel Cells 9 (5) (2009) 499–505.

[3] H. Ostadi, K. Jiang, P. Rama, Y. Liu, R. Chen, 3D reconstruction of a gas diffusion layer and a microporous layer, J. Membr. Sci. 351 (1–2) (2010) 69–74.

[4] Y. Gao, X.X. Zhang, P. Rama, Y. Liu, R. Chen, H. Ostadi, K. Jiang, Modelling fluid flow in the gas diffusion layers in PEMFC using the multiple relaxation time Lattice Boltzmann method, Fuel Cells 12 (3) (2012) 365–381.

[5] D.H. Rothman, J.M. Keller, Immiscible cellular-automaton fluids, J. Stat. Phys. 52 (3–4) (1988) 1119–1127.

[6] A.K. Gunstensen, D.H. Rothman, S. Zaleski, G. Zanetti, Lattice Boltzmann model of immiscible fluids, Phys. Rev. A 43 (8) (1991) 4320–4327.

[7] A.K. Gunstensen, D.H. Rothman, Microscopic modeling of immiscible fluids in three dimensions by a lattice Boltzmann method, Europhys. Lett. 18 (2) (1992) 157.

[8] G.R. Mcnamara, G. Zanetti, Use of the Boltzmann equation to simulate lattice gas automata, Phys. Rev. Lett. 61 (20) (1988) 2332–2335.

[9] F.J. Higuera, J. Jimenez, Boltzmann approach to lattice gas simulations, Europhys. Lett. 9 (7) (1989) 663–668.

[10] X. He, G.D. Doolen, Thermodynamics foundations of kinetic theory and lattice Boltzmann models for multiphase flows, J. Stat. Phys. 107 (1–2) (2002) 309–328.

[11] D.W. Grunau, S.Y. Chen, K. Eggert, A lattice Boltzmann model for multiphase fluid flows, Phys. Rev. A 5 (10) (1993) 2557–2563.

[12] B. Ahrenholz, J. Tolke, P. Lehmann, A. Peters, A. Kaestner, M. Krafczyk, W. Durner, Prediction of capillary hysteresis in a porous material using lattice Boltzmann methods and comparison to experimental data and a morphological pore network model, Adv. Water Resour. 31 (2008) 1151–1173.

[13] X. Shan, H. Chen, Lattice Boltzmann model for simulating flows with multiple phases and components, Phys. Rev. E 47 (3) (1993) 1815–1819.

[14] X. Shan, H. Chen, Simulation of nonideal gases and liquid–gas phase transitions by the lattice Boltzmann equation, Phys. Rev. E 49 (4) (1994) 2941–2948.

[15] X. Shan, G. Doolen, Diffusion in a multi-component lattice Boltzmann equation model, Phys. Rev. E 54 (4) (1996) 3614–3620.

[16] N. Martys, J.F. Douglas, Critical properties and phase separation in lattice Boltzmann fluid mixtures, Phys. Rev. E 63 (3) (2001) 031205.

[17] S.L. Hou, X.W. Shan, Q.S. Zou, G.D. Doolen, W.E. Soll, Evaluation of two lattice Boltzmann models for multiphase flows, J. Comput. Phys. 138 (2) (1997) 695–713.

[18] S. Leclaire, M. Reggio, J.Y. Trepanier, Numerical evaluation of two recoloring operators for an immiscible two-phase flow lattice Boltzmann model, Appl. Math. Model. 36 (5) (2012) 2237–2252.

[19] H.B. Huang, L. Wang, X.Y. Lu, Evaluation of three lattice Boltzmann models for multiphase flows in porous media, Comput. Math. Appl. 61 (12) (2011) 3606–3617.

[20] M.R. Swift, W.R. Osborn, J.M. Yeomans, Lattice Boltzmann simulation of nonideal fluids, Phys. Rev. Lett. 75 (5) (1995) 830–833.

[21] M.R. Swift, W.R. Osborn, J.M. Yeomans, Lattice Boltzmann simulations of liquid–gas and binary fluid systems, Phys. Rev. E 54 (5) (1996) 5041–5052.

[22] X. He, S. Chen, R. Zhang, A lattice Boltzmann scheme for incompressible multiphase flow and its application in simulation of Rayleigh–Taylor instability, J. Comput. Phys. 152 (2) (1999) 642–663.

[23] T. Lee, C.L. Lin, A stable discretization of the lattice Boltzmann equation for simulation of incompressible two-phase flows at high density ratio, J. Comput. Phys. 206 (1) (2005) 16–47.

[24] H.W. Zheng, C. Shu, Y.T. Chew, A lattice Boltzmann model for multiphase flows with large density ratio, Journal of Computational Physics 218 (1) (2006) 353–371.

[25] T. Inamuro, T. Ogata, S. Tajima, N. Konishi, A lattice Boltzmann method for incompressible two-phase flows with large density differences, Journal of Computational Physics 198 (2) (2004) 628–644.

[26] P.P. Mukherjee, C.Y. Wang, Mesoscopic modelling of two-phase behavior and flooding phenomena in polymer electrolyte fuel cells, Electrochim. Acta 54 (27) (2009) 6861–6875.

[27] X.D. Niu, T. Munekata, S.A. Hyodo, K. Suga, An investigation of water–gas transport processes in the gas-diffusion-layer of a pem fuel cell by a multiphase multiple-relaxation-time lattice Boltzmann model, J. Power Sources 172 (2) (2007) 542–552.

[28] L. Hao, P. Cheng, Lattice Boltzmann simulation of liquid droplet dynamic behaviour on a hydrophobic surface of a gas flow channel, J. Power Sources 190 (2) (2009) 435–446.

[29] D. D'Humieres, I. Ginzburg, M. Krafczyk, P. Lallemand, L. Luo, Multiple-relaxation-time lattice Boltzmann models in three dimensions, Phil. Trans. R. Soc. A 360 (2002) 437–451.

[30] I. Ginzburg, Variably saturated flow with the anisotropic lattice Boltzmann method, Comput. & Fluids 35 (8–9) (2006) 831–848.

[31] Z. Yu, L.S. Fan, An interaction potential based lattice Boltzmann method with adaptive mesh refinement (AMR) for two-phase flow simulation, Journal of Computational Physics 228 (17) (2009) 6456–6478.

[32] B. Ahrenholz, J. Tölke, M. Krafczyk, Lattice Boltzmann simulations in reconstructed parametrized porous media, Int. J. Comput. Fluid Dyn. 20 (9) (2006) 369–377.

[33] M. Bouzidi, M. Firdaouss, P. Lallemand, Momentum transfer of a lattice-Boltzmann fluid with boundaries, Phys. Fluids 13 (2001) 3452–3459.

[34] Q.S. Zou, X.Y. He, On pressure and velocity boundary conditions for the lattice Boltzmann BGK model, Phys. Fluids 9 (6) (1997) 1591–1598.